

Convective radial energy flux due to resonant magnetic perturbations and magnetic curvature at the tokamak plasma edge

F.A. Marcus,^{1,2, a)} P. Beyer,² G. Fuhr,² A. Monnier,² and S. Benkadda²

¹⁾*Institute of Physics at University of São Paulo C.P. 66318, 05315-970 São Paulo, S.P., Brazil*

²⁾*Aix-Marseille Université, CNRS, PIIM UMR 7345, 13397 Marseille Cedex 20, France*

With the resonant magnetic perturbations (RMPs) consolidating as an important tool to control the transport barrier relaxation, the mechanism on how they work is still a subject to be clearly understood. In this work we investigate the equilibrium states in the presence of RMPs for a reduced MHD model using 3D electromagnetic fluid numerical code (EMEDGE3D) with a single harmonic RMP (single magnetic island chain) and multiple harmonics RMPs in cylindrical and toroidal geometry. Two different equilibrium states were found in the presence of the RMPs with different characteristics for each of the geometries used. For the cylindrical geometry in the presence of a single RMP, the equilibrium state is characterized by a strong convective radial thermal flux and the generation of a mean poloidal velocity shear. In contrast, for toroidal geometry the thermal flux is dominated by the magnetic flutter. For multiple RMPs, the high amplitude of the convective flux and poloidal rotation are basically the same in cylindrical geometry, but in toroidal geometry the convective thermal flux and the poloidal rotation appear only with the islands overlapping of the linear coupling between neighbouring poloidal wavenumbers m , $m - 1$, $m + 1$.

^{a)}albertus@if.usp.br

I. INTRODUCTION

The key to improve plasma confinement in tokamaks at high temperature and density lies on the transport barriers achieved in so called H-mode regimes, first discovered on ASDEX¹ in the early 1980's. This high energy confinement mode (H-mode) with a steep pressure gradient at the edge represents out of few percent of the plasma radius in toroidal magnetic systems. In this regime the plasma pressure drops sharply over a narrow layer in the middle of the plasma edge. Once the H-mode is settled, this pressure gradient tends to increase with time until the peeling-ballooning instability leads to a turbulent state triggering the Edge Localized Modes (ELMs), which release the transport barriers in a time shot compared to the the energy confinement time τ_C .^{2,3} ELMs are periodic fast bursts of hot dense plasma on a fast time scale ($\sim 25-300\mu s$) and low amplitude, followed by expulsion of edge plasma and MHD activity, leading to confinement degradation⁴. Along with the fast barrier relaxation event, a turbulent transport through the barrier strongly increases and the pressure gradient drops down reaching a new configuration and then the barrier builds up again on a slow collisional time scale.

Turbulence simulations of transport barrier relaxations at the tokamak plasma edge have revealed that the control of such relaxations by RMPs is attributed to a local erosion of the barrier⁵⁻⁷. This erosion at the resonance position is known to be caused - at least partly - by the enhancement of the radial heat flux in presence of the RMP due to the strong parallel heat flow along perturbed field lines as is the so called magnetic flutter flux⁸. However, in the presence of magnetic curvature, an additional transport mechanism exists and is linked to stationary convection cells associated with the magnetic islands induced by RMPs^{5,6}. In presence of a mean poloidal velocity shear, this additional convective transport can be considerably high and even larger than the thermal flux from the magnetic flutter flux⁷. This previous result has been obtained in the frame of an electrostatic model.

We show here by numerical simulations in the frame of a 3D electromagnetic fluid turbulence model (EMEDGE3D)⁹ and in the basic situation without turbulent fluctuations and without imposed mean velocity shear that two different equilibrium plasma states exists in presence of a RMP. The first regime is characterized by the absence of mean poloidal flow and a low level of convective transport. The second regime shows mean poloidal rotation and large convective transport. Here we show how these two equilibria depend on magnetic

curvature and RMP amplitude. Interestingly, in the case of cylindrical curvature, the simple equilibrium without mean poloidal rotation and without considerable convective transport is found to be unstable such that the plasma evolves self-consistently to the poloidally rotating state where large convective transport is present. In the case of toroidal curvature, the simple equilibrium is found to be stable. A detailed stability analysis is presented.

In section II, the dimensionless 3D model of partial differential equations is presented with the profiles used for the code EMEDGE3D. In section III, the helical equilibrium states of the plasma driven by the RMP coils is derived for the cylindrical case and compared with simulations, for then analyse the results obtained in terms of the islands width in section IV. We show the different equilibrium states obtained with the toroidal geometry with multiple harmonics RMPs in section V, then we detach the main results of the work in section VI as a conclusion.

II. 3D PLASMA-RMP MODEL

Following Beyer¹⁰ and Fuhr⁹, we introduce three reduced normalized magneto-hydrodynamical PDEs with source J_{RMP} for the strength of the RMP currents. The equations are used to study the spatio-temporal behaviour of the three-dimensional fields of plasma pressure p , electrostatic potential ϕ and magnetic flux ψ .

$$\partial_t \nabla_{\perp}^2 \phi + \{\phi, \nabla_{\perp}^2 \phi\} = -\alpha^{-1} \nabla_{\parallel} \nabla_{\perp}^2 \psi - \mathbf{G}p + \nu \nabla_{\perp}^4 \phi, \quad (1)$$

$$\partial_t p + \{\phi, p\} = \delta_c \mathbf{G}\phi + \chi_{\parallel} \nabla_{\parallel}^2 p + \nabla_{\perp} \cdot [\chi_{\perp}(x) \nabla_{\perp} p] + S(x), \quad (2)$$

$$\partial_t \psi = -\nabla_{\parallel} \phi + \alpha^{-1} \nabla_{\perp}^2 \psi - \alpha^{-1} J_{RMP}. \quad (3)$$

In toroidal coordinates (r, θ, φ) and in a slab geometry (x, y, z) in the vicinity of a reference surface $r = r_0$ at the plasma edge, i.e. $x = (r - r_0)/\xi_{\text{bal}}$, $y = r_0\theta/\xi_{\text{bal}}$, $z = R_0\varphi/L_s$, the normalized operators are

$$\begin{aligned} \nabla_{\parallel} &= \partial_z + (\kappa/q_0 - x) \partial_y - \{\psi, \cdot\} \quad \text{with} \quad \kappa = \frac{L_s r_0}{R_0 \xi_{\text{bal}}}, \\ \nabla_{\perp}^2 &= \partial_x^2 + \partial_y^2, \\ \{\phi, \cdot\} &= \partial_x \phi \partial_y - \partial_y \phi \partial_x, \\ \mathbf{G} &= \begin{cases} \sin \theta \partial_x + \cos \theta \partial_y, & \text{in case of toroidal curvature} \\ g_0 \partial_y, & \text{in case of cylindrical curvature} \end{cases}. \end{aligned}$$

Here, $q_0 = q(r_0)$ is the safety factor at the reference surface, R_0 is the major radius of the magnetic axis and L_s is the magnetic shear length. Lengths parallel (\parallel) and perpendicular (\perp) to the unperturbed magnetic field are normalized by L_s and ξ_{bal} , respectively, and time is normalized by τ_{int} , where the resistive ballooning radial correlation length ξ_{bal} and the interchange time τ_{int} are given by

$$\xi_{\text{bal}} = \left(\frac{L_p}{\tau_e c_s} \frac{m_e}{m_i} \right)^{\frac{1}{2}} \frac{L_s}{L_p} \left(\frac{L_p}{R_0} \right)^{\frac{1}{4}} \rho_s \quad \text{and} \quad \tau_{\text{int}} = \frac{(L_p R_0)^{\frac{1}{2}}}{\sqrt{2} c_s},$$

where m_e/m_i is the ratio of the electron to the ion mass, and τ_e , c_s , L_p , ρ_s are reference values of the electron collision time, the sound speed, the pressure gradient length, and the ion Larmor radius at electron temperature, respectively. For a collisional tokamak plasma edge, one typically finds $\xi_{\text{bal}} \sim \rho_s$ and $\tau_{\text{int}} \sim 10L_p/c_s$.

The dimensionless ballooning pressure gradient coefficient $\alpha = (\beta/L_p)(L_s^2/R_0)$ is similar to the normalized pressure gradient α_{MHD} widely used in MHD tokamak stability theory [$\alpha_{\text{MHD}} = \alpha(q_0 R_0/L_s)^2$], where β is the ratio of plasma pressure to magnetic pressure. The parallel and perpendicular heat conductivity coefficients χ_{\parallel} and χ_{\perp} are normalized by L_s^2/τ_{int} and $\xi_{\text{bal}}^2/\tau_{\text{int}}$, respectively. Therefore, a ratio of the normalized coefficients of $\chi_{\parallel}/\chi_{\perp} \sim 1$, corresponds to a ratio of the dimensional coefficients of $L_s^2/\xi_{\text{bal}}^2 \sim 10^7 - 10^8$. In the present simulations, we use $\alpha = 0.1$, $\nu = \chi_{\perp} = 0.93$, $\chi_{\parallel} = 1$ and the curvature parameter $\delta_c = \frac{5}{3} 2L_p/R_0$ is set to $\delta_c = 0.01$.

The main computational domain corresponds to the volume delimited by the toroidal surfaces characterized by $q = 2.5$ and $q = 3.5$, respectively, and including the reference surface $q = q_0 = 3$. Here, a linear $1/q$ profile is assumed, and $\xi_{\text{bal}}/r_0 = 1/500$, $L_s/R_0 = 1$ for the reference parameters. The complete computational domain is slightly larger and delimited by $x_{\text{min}} < x_{q=2.5}$ and $x_{\text{max}} > x_{q=3.5}$. The source S is located in the inner buffer zone $x_{\text{min}} < x < x_{q=2.5}$ and gives rise to a constant incoming energy flux, $Q_{\text{tot}} = \int_{x_{\text{min}}}^{x_{q=2.5}} S dx$ from the plasma center into the main computational domain. The helical current $J_0(x)$

$$J_{\text{RMP}} = J_0(x) \cos \zeta \tag{4}$$

is located in the outer buffer zone $x_{q=3.5} < x < x_{\text{max}}$ (Fig. 2a). Here, the RMP coil structure is a function of the helical angle

$$\zeta = m_0 \theta - n_0 \varphi = \frac{m_0 \xi_{\text{bal}}}{r_0} y - \frac{n_0 L_s}{R_0} z.$$

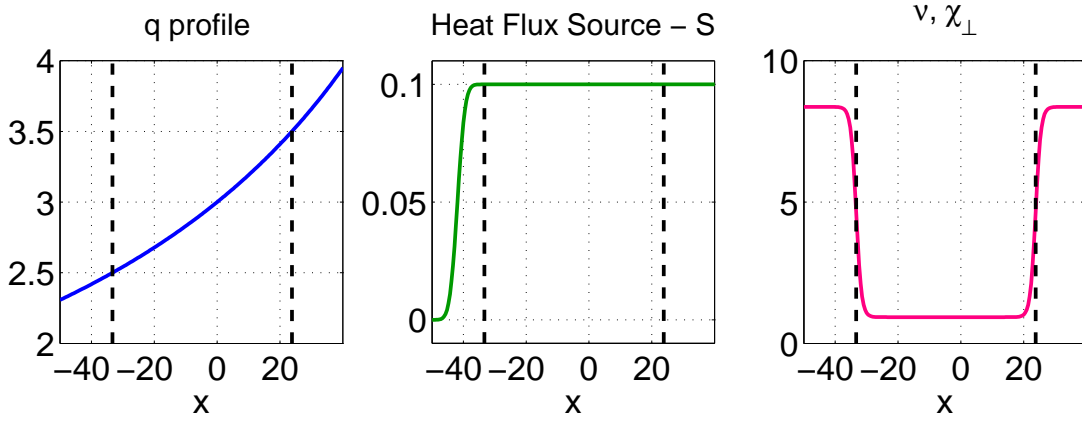


FIG. 1. Radial profiles of the safety factor (a), the incoming energy flux (b) and perpendicular diffusivity and viscosity (c) as a function of the normalized radial coordinate x . The vertical dashed lines delimit the main computational domain, which is between $x = -33.3$ and $x = 23.8$ and where $q = 2.5$ and $q = 3.5$, respectively. The left part is associated to the incoming energy flux from the core and the right to the external magnetic perturbations, both defined as buffer zone.

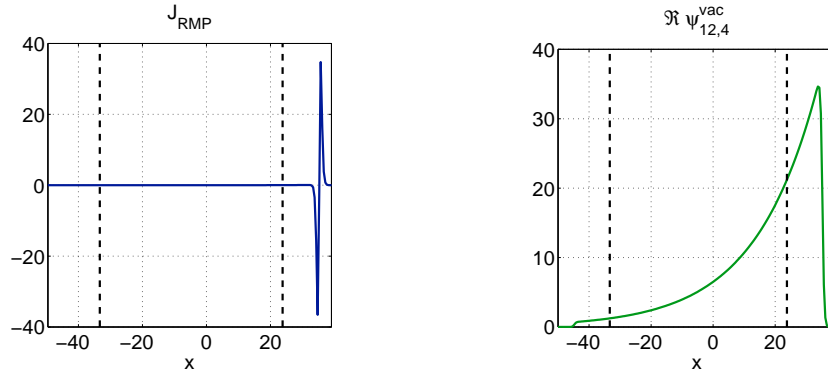


FIG. 2. Radial profiles of (a) the amplitude $J_0(x)$ of the external helical current and (b) the resulting vacuum magnetic perturbation $\psi_{12,4}$.

Here we choose the regime RMP coil with $(m_0, n_0) = (12, 4)$, which the external current induces a magnetic perturbation resonant at $q = q_0 = 3$ as shown in Fig. 2b.

The pressure profile $\bar{p}(x, t) = \langle p \rangle_{y,z}$ evolves self consistently according to the energy transport equation [the toroidal and poloidal average $\langle \cdot \rangle_{yz}$ of (2)],

$$\partial_t \bar{p} = -\partial_x (Q_{\text{conv}} + Q_{\text{coll}} + Q_{\delta B}) + S, \quad (5)$$

with $Q_{\text{conv}} = \langle p \partial_y \phi \rangle_{y,z}$, $Q_{\text{coll}} = -\chi_{\perp} \partial_x \bar{p}$, $Q_{\delta B} = -\chi_{\parallel} \langle \partial_y \psi \nabla_{\parallel} p \rangle_{y,z}$. In a stationary state,

integrating Eq. 5 in the radial direction leads to the energy flux balance

$$Q_{\text{conv}}(x) + Q_{\text{coll}}(x) + Q_{\delta B}(x) = Q_{\text{tot}} \quad \text{for } x \geq x_{q=2.5} \quad (6)$$

for a steady state.

III. EQUILIBRIUM STATES IN PRESENCE OF RMP

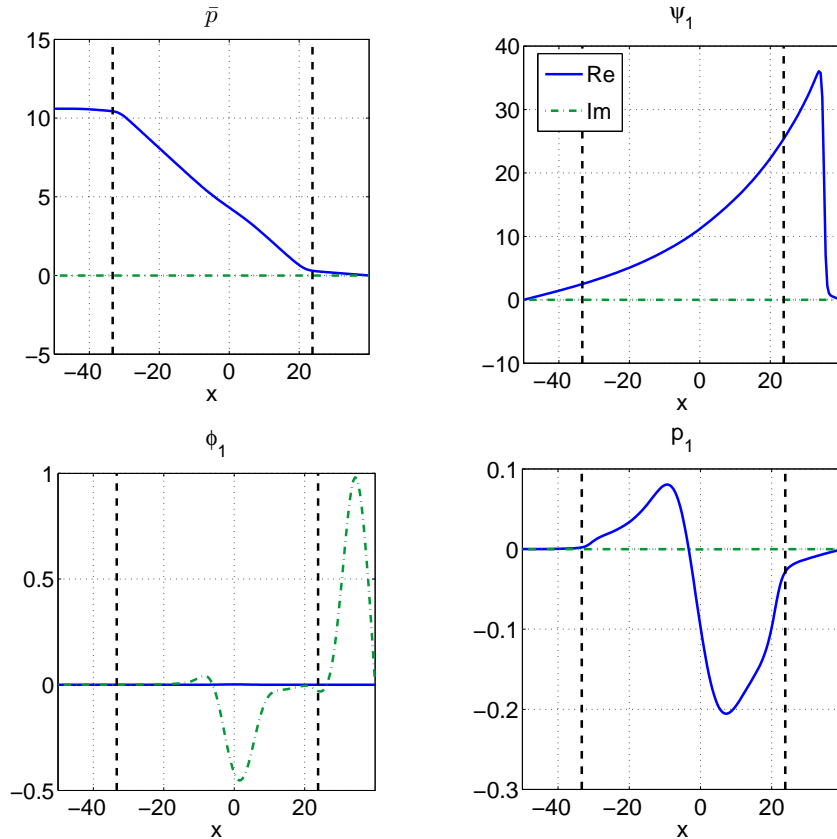


FIG. 3. Radial profiles of the fields \bar{p} , ϕ_1 , p_1 and ψ_1 corresponding to the calculated helical equilibrium described in Eq. (13). The magnetic perturbation is in phase with the external current and the plasma is not rotating ($\bar{v}_E = \partial_y \bar{\phi} = 0$), but this equilibrium is unstable according to the results obtained with numerical simulations. The dashed vertical lines mark the location of the rational magnetic surfaces with $q = 5/2$ and $q = 7/2$.

In the following, for a given RMP coil, two different helical equilibrium states of the plasma are obtained by the numerical calculations we first deduce analytically their main properties in the case of cylindrical curvature. In this case, there is no linear coupling

between neighbouring poloidal wavenumbers m , $m - 1$, $m + 1$, etc., and the equilibrium can be assumed to be of the form

$$\begin{pmatrix} \phi_{\text{eq}} \\ p_{\text{eq}} \\ \psi_{\text{eq}} \end{pmatrix} = \begin{pmatrix} \bar{\phi}(x) \\ \bar{p}(x) \\ 0 \end{pmatrix} + \begin{pmatrix} \phi_1(x) \\ p_1(x) \\ \psi_1(x) \end{pmatrix} \exp(i\zeta) + c.c. , \quad (7)$$

where the bar and the index "1" designate respectively the axisymmetric and the $(m, n) = (m_0, n_0) = (12, 4)$ components, in which

$$(\phi_1, p_1, \psi_1) \equiv (\phi_{m_0, n_0}, p_{m_0, n_0}, \psi_{m_0, n_0}) \equiv (\phi_{12,4}, p_{12,4}, \psi_{12,4}) .$$

Inserting the expression (7) in Eq. (1)–(3) yields the following set of five coupled equations for $\bar{\phi}$, \bar{p} , ϕ_1 , p_1 and ψ_1 ,

$$-\frac{1}{2}k_y \partial_x \Im [\phi_1 (\partial_x^2 - k_y^2) \phi_1^*] = -\frac{1}{2\alpha} k_y \partial_x \Im [\psi_1 (\partial_x^2 - k_y^2) \psi_1^*] + \nu \partial_x^4 \bar{\phi} , \quad (8)$$

$$2k_y \partial_x \Im (\phi_1 p_1^*) = -2\chi_{\parallel} k_y^2 \partial_x [x \Re (\psi_1 p_1^*) - |\psi_1|^2 \partial_x \bar{p}] + \chi_{\perp} \partial_x^2 \bar{p} + S . \quad (9)$$

$$i [\partial_x \bar{\phi} (\partial_x^2 - k_y^2) \phi_1 - \phi_1 \partial_x^3 \bar{\phi}] = -ig_0 p_1 + \frac{i}{\alpha} x (\partial_x^2 - k_y^2) \psi_1 + \frac{\nu}{k_y} (\partial_x^2 - k_y^2)^2 \phi_1 , \quad (10)$$

$$\begin{aligned} \frac{i}{k_y} (p_1 \partial_x \bar{\phi} - \phi_1 \partial_x \bar{p}) &= \frac{i}{k_y} \delta_c g_0 \phi_1 - \chi_{\parallel} x^2 p_1 + \chi_{\parallel} x \psi_1 \partial_x \bar{p} + 2i\chi_{\parallel} \psi_1 \partial_x^2 (\psi_1 \Im p_1) \\ &+ \chi_{\parallel} (\psi_1 \partial_x - 2\partial_x \psi_1) \partial_x (\psi_1 p_1) + \frac{\chi_{\perp}}{k_y^2} (\partial_x^2 - k_y^2) p_1 , \end{aligned} \quad (11)$$

$$0 = ik_y x \phi_1 + ik_y \psi_1 \partial_x \bar{\phi} + \frac{1}{\alpha} (\partial_x^2 - k_y^2) \psi_1 . \quad (12)$$

Here, $\Re f = (f + f^*)/2$ and $\Im f = (f - f^*)/2i$. Eqs. (8)–(12) admit a symmetric solution corresponding to a helical equilibrium where the induced magnetic perturbation and the associated pressure perturbation are in phase with the external current (4), i.e. $\Im \psi_1 = 0$, $\Im p_1 = 0$, and the potential variation is in phase quadrature, $\Re \phi_1 = 0$. In this equilibrium, the poloidal rotation is zero, $\bar{v}_E = \partial_y \bar{\phi} = 0$. In summary, the solutions of Eq. (8)–(12) reduces to

$$\begin{pmatrix} \phi_{\text{eq}}^{(1)} \\ p_{\text{eq}}^{(1)} \\ \psi_{\text{eq}}^{(1)} \end{pmatrix} = \begin{pmatrix} 0 \\ \bar{p}(x) \\ 0 \end{pmatrix} + \begin{pmatrix} -2\phi_1^I(x) \sin \zeta \\ 2p_1^R(x) \cos \zeta \\ 2\psi_1^R(x) \cos \zeta \end{pmatrix} , \quad (13)$$

where ϕ_1^I , p_1^R and ψ_1^R are real fields corresponding to the imaginary (I) and real (R) parts of ϕ_1 , p_1 and ψ_1 , respectively. Typical radial profiles of \bar{p} , ϕ^I , p^R and ψ^R are shown in Fig. 3. Note that there is a non-vanishing convective flux Q_{conv} associated with the equilibrium (13),

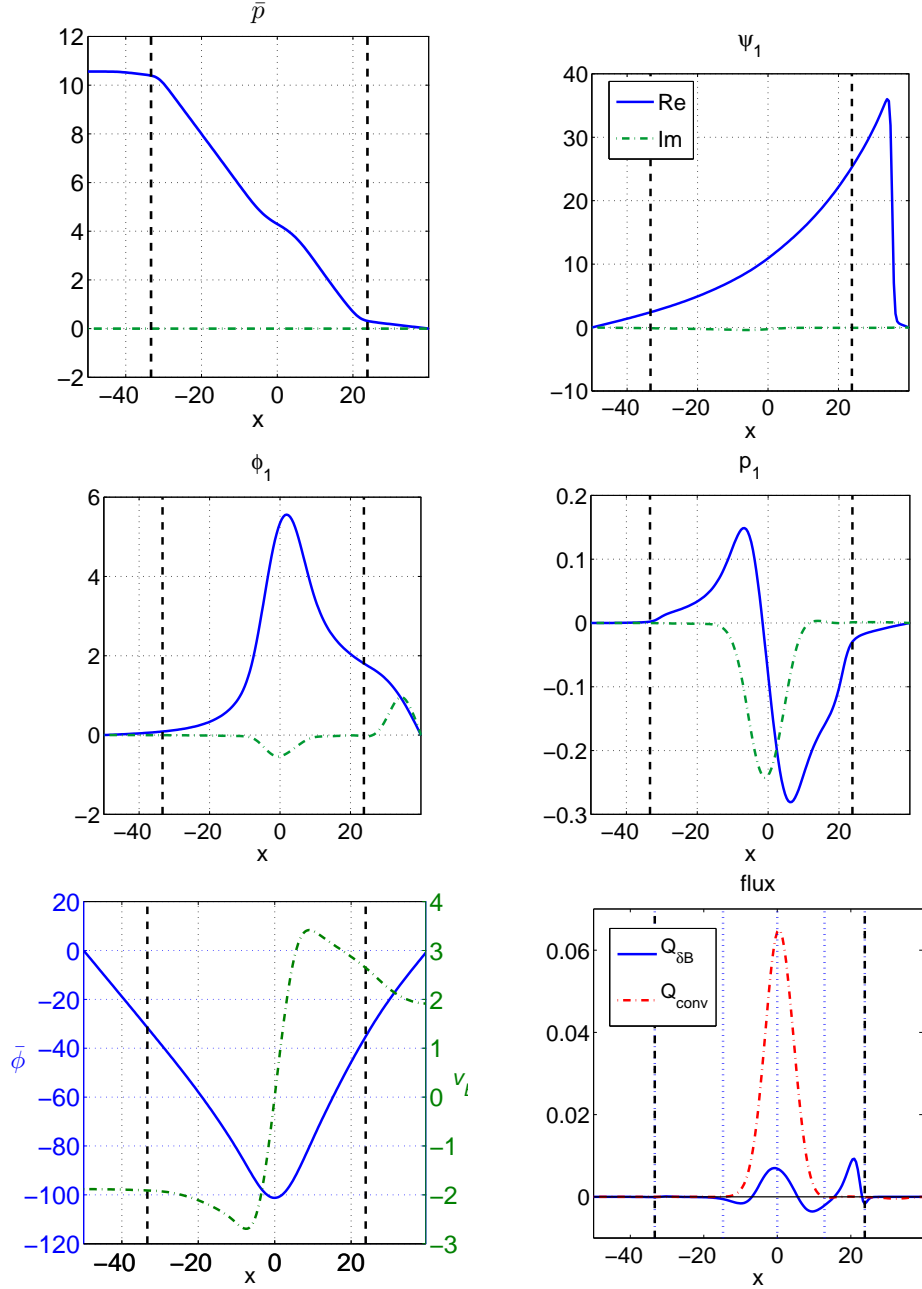


FIG. 4. (Color online) Radial profiles of the fields \bar{p} , ψ_1 , p_1 , ϕ_1 , the poloidal rotation $\bar{v}_E = \partial_y \bar{\phi}$ and the fluxes Q_{conv} , $Q_{\delta B}$ corresponding to the stable helical equilibrium. The magnetic perturbation is phase shifted with respect to the external current.

as the pressure and potential perturbations are phase shifted by $\pi/2$. However, in typical situations as the one illustrated in Fig. 3, this convective flux is found to be much smaller than the magnetic flutter flux $Q_{\delta B}$. Stable helical equilibrium states of the plasma in presence of the RMP can be calculated numerically by integrating Eq. (1)–(3) in time starting with

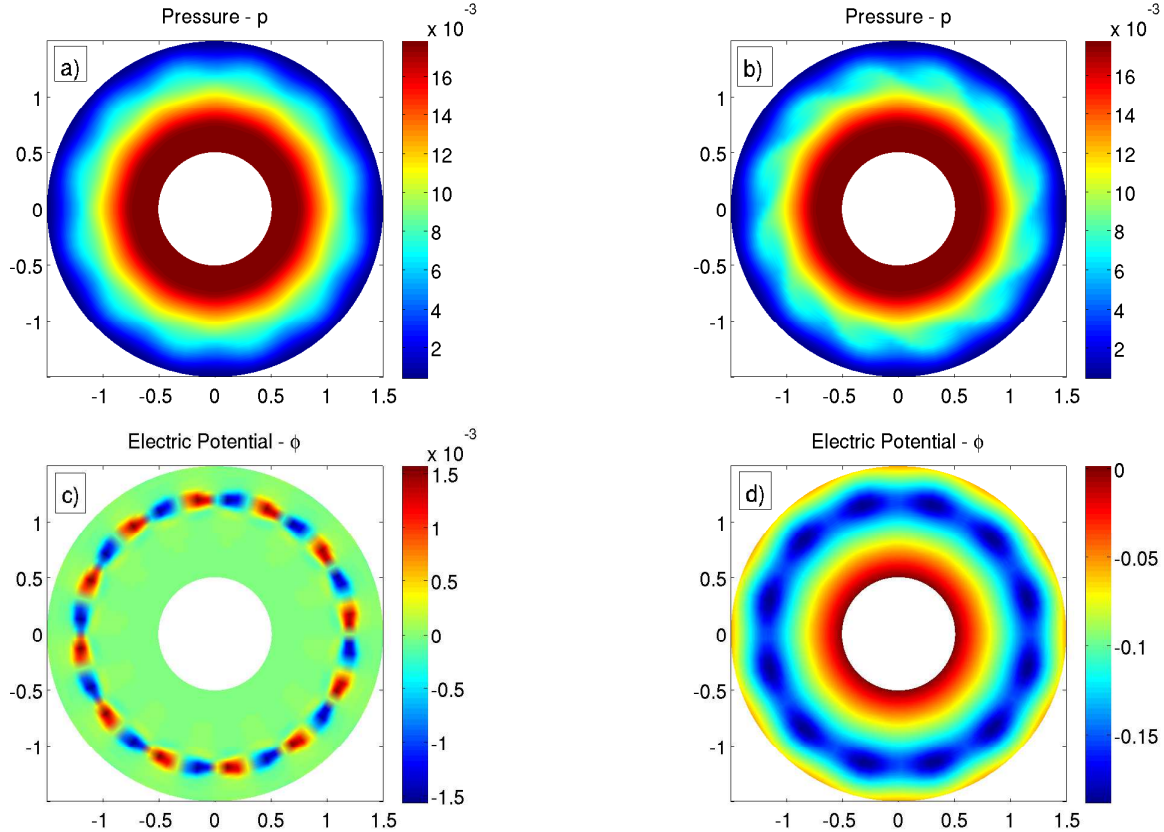


FIG. 5. (Color online) Two dimensional maps of the pressure p and the non-axisymmetric part of potential $\phi - \bar{\phi}$ corresponding to the two different equilibrium states in cylindrical geometry. Pictures a) and c) depict the pressure and electric potential profiles for the case described by system in equilibrium in Eq. (13) with the profiles shown on Fig. 3. This system evolves to the state depicted on frames b) and d) with poloidal rotation, which the phase-shift between p and $\partial\phi$ play the role to the high convective flux and the poloidal rotation.

low level noise for all fields, providing that the pressure gradient $\partial_x \bar{p}$ stays below the resistive ballooning instability limit. This is guaranteed here by choosing a sufficiently low value of the total energy flux Q_{tot} . However, with this convergence method, the symmetric equilibrium state (13) can only be obtained when explicitly forcing no rotation. This means that the symmetric equilibrium is unstable. This property will be discussed in the next section. When the temporal evolution is calculated self-consistently including poloidal rotation, the system evolves to a new helical stationary state with non vanishing sheared plasma rotation. We call this new equilibrium here *rotating state* and it is characterized by: A. a phase shift between the external current and the magnetic perturbation induced in the plasma and B. a large

convective flux $Q_{\text{conv}} \gg Q_{\delta B}$. Typical radial profiles of the axisymmetric components as well as the helical amplitudes and the fluxes are shown in Fig. 4. Note that the rotation velocity vanishes close to the resonant surface which is consistent with a nearly complete penetration of the magnetic perturbation¹¹, i.e. the amplitudes of the $\psi_{12,4}(x)$ at the resonance surface $x = 0$ are similar in both equilibria and close to the maximum value corresponding to the vacuum case. We may summarise the fields in the rotating steady state as

$$\hat{\psi}_{12,4}^{\text{rotation state}} \approx \hat{\psi}_{12,4}^{\text{symmetric state}} \approx \hat{\psi}_{12,4}^{\text{vacuum}} , \quad \text{where} \quad \hat{\psi}_{12,4} = |\psi_{12,4}(x=0)| . \quad (14)$$

Note also that due to the strong convective flux, the flattening of the pressure profile on the resonant surface is significantly more pronounced in the rotating state compared with the symmetric state (cf. Figs. 3a and 4a). Two dimensional maps of the pressure p and the non-axisymmetric part of potential $\phi - \bar{\phi}$ corresponding to the two different equilibrium states are shown in Fig. 5. The periodic structure that corresponds to the flattening of the pressure on the magnetic islands is symmetric in the symmetric state (Fig. 5a) and distorted in the rotation state (Fig. 5b) from the shear flow. The potential structure together with the pressure structure, as illustrated in Fig. 5d, is responsible for the strong convective flux in the rotation state. Note that with increasing amplitude of the external RMP current, both the magnetic flutter flux and the convective flux increase in the stable rotating equilibrium, but the convective flux is always larger than the thermal flux produced by magnetic flutters as shown in Fig. 6.

IV. TRANSITION TO THE ROTATING STATE WITH STRONG CONVECTIVE FLUX

The instability of the symmetric equilibrium and the transition to the second helical state described above can be illustrated by performing a time integration in two successive phases and following the evolution of the convective and magnetic flutter fluxes at the resonant surface (Fig. 7a). In an early phase of the integration (from $t = 0.05 \cdot 10^4$ on), the rotation is forced to zero and the system is rapidly evolving to the stationary state obtained in Eq. (13), where the convective flux Q_{conv} is much smaller than the flutter flux $Q_{\delta B}$. Then, from $t = 8000$ on, we release the constraint on the poloidal rotation and the system evolves self-consistently to the rotating state characterized by $Q_{\text{conv}} \gg Q_{\delta B}$. The

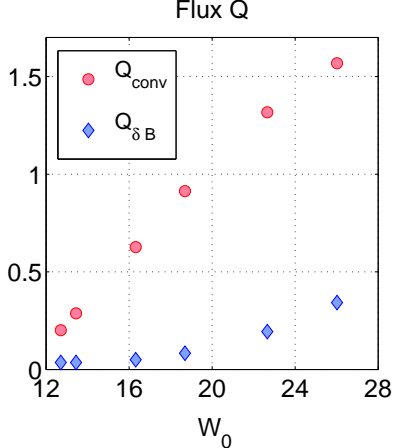


FIG. 6. (Color online) Radially integrated convective and flutter fluxes for the cylindrical case, $Q_{\text{conv}} = \int_{q=2.5}^{q=3.5} Q_{\text{conv}}(x) dx$ and $Q_{\delta B} = \int_{q=2.5}^{q=3.5} Q_{\delta B}(x) dx$, as a function of a single magnetic perturbation amplitude expressed in terms of the vacuum island width W_0 . Even for low values of external resonant magnetic perturbation ψ_0 (small island width W_0), Q_{conv} is higher than $Q_{\delta B}$.

instability of the symmetric equilibrium can be characterized by the growth rate of a small perturbations of this equilibrium. The growth rate can be determined in the numerical experiment described above. A series of such numerical simulations for different amplitudes of the external magnetic perturbation reveals that the growth rate is nearly constant up to a critical value of the RMP perturbation level. Above this level, the growth rate is strongly increasing with the external perturbation amplitude. This is illustrated in Fig. 7b where the growth rate is plotted against the magnetic island width W linked to the perturbation amplitude via

$$W = 4\sqrt{2\hat{\psi}_{12,4}}. \quad (15)$$

The time growth rate of Q_{conv} strongly increases for island widths $W > 34$. In that case, the half-width of the island $W/2 > 17$ approaches the distance between the resonant surface and the external boundary of the main computational domain $x_{q=3.5} - x_{q=3} = 23$ and the island likely is influenced by the boundary. Also, higher order harmonics become significant for $W > W_c \approx 22$, where the critical island width is given by⁸ $W_c = [(8/m_0)(r_0/\xi)]^{1/2} (\chi_{\perp}/\chi_{\parallel})^{1/4}$. As illustrated in Fig. 8, for $W = 18$ the amplitude of the second order $(m, n) = (24, 8)$ mode is one order of magnitude lower than the amplitude of the main harmonics but for $W = 36.5$, the second harmonic is only lower by a factor of 0.3.

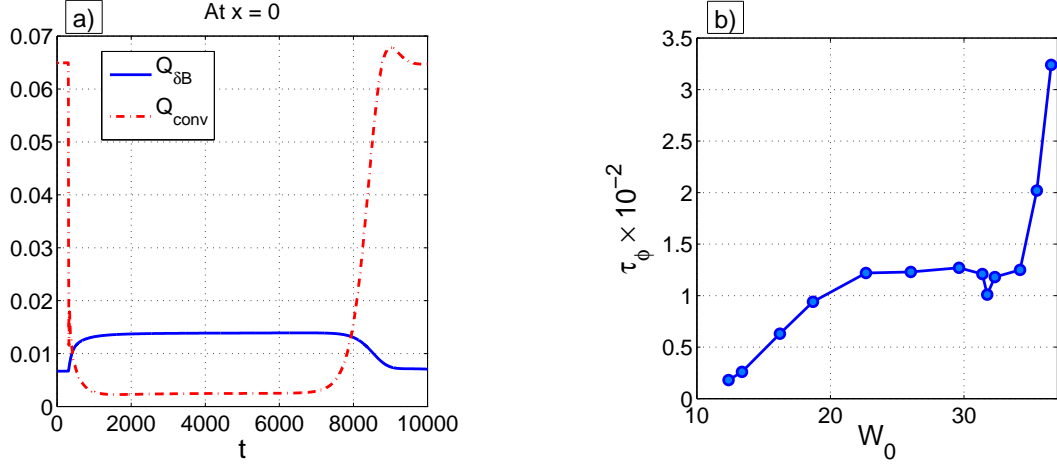


FIG. 7. (Color online) - (a) Evolution of the convective (red dot dashed line) and magnetic flutter (blue line) fluxes. Forcing the rotation to zero, the convective flux decreases and the system responds increasing the flux of the magnetic flutter. Releasing the constrain, the system evolves to a stable condition with Q_{conv} bigger than $Q_{\delta B}$. (b) The growth rate of the convective flux plotted against the magnetic island width W_0 .

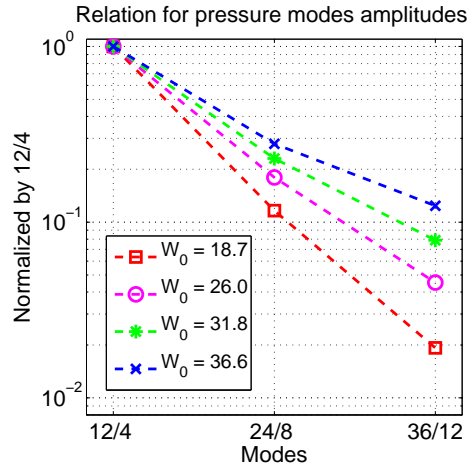


FIG. 8. (Color online) Relation for resonant pressure modes amplitudes. Larger the island width W_0 , which means higher resonant magnetic perturbation, more intense the harmonics modes become, contributing to the increase of Q_{conv} and poloidal rotation effects.

V. STABLE ROTATING STATE IN TOROIDAL GEOMETRY WITH MULTIPLE RMPS

Toroidal curvature gives rise to linear coupling between $m - 1$, m , and $m + 1$ modes. In particular, in the vorticity equation (1) a (m, n) harmonic of the pressure p couples to $(m - 1, n)$ and $(m + 1, n)$ harmonics of the electrostatic potential ϕ . If a self-consistent state with rotation and convective transport similar to the one shown in the Fig. 4 exists in toroidal geometry, then the state involve multiple harmonics. We therefore induce a multiple harmonics RMP with poloidal wavenumbers $m = 10, 11, 12, 13, 14$ and toroidal wavenumber $n = 4$. In order to compare with the results shown above, we first apply the multiple harmonics RMP in the cylindrical curvature case. As illustrated in Fig. 9, a stable equilibrium with rotation and important convective flux is recovered in this case. The plasma self-organizes such that the rotation velocity vanishes close to the resonant surfaces $q = 11/4, 12/4, 13/4$. The convective and magnetic flutter fluxes show local maxima close to these resonant surfaces (Fig. 9b). The width of the $(12, 4)$ island is $W_{12,4} = 18.5$ and the width of the closest neighbouring island $(13, 4)$ is $W_{13,4} = 18.4$, so the corresponding Chirikov overlapping parameter¹² is

$$\sigma = \frac{W_{12,4} + W_{13,4}}{2x_{q=3.25}} \approx 1.4 .$$

The islands therefore are overlapping, but this overlapping is weak enough such that distinct local maxima are observed for the Q_{conv} and $Q_{\delta B}$ fluxes, as shown in Fig. 9b. When applying a multiple harmonics RMPs in the toroidal curvature case, the plasma also evolves to a stable equilibrium with rotation and strong convective flux. This is illustrated in Fig. 11, which may be compared with Fig. 9. Differently from the cylindrical case in which a poloidal rotation is induced for all values of RMPs amplitudes, the poloidal rotation in toroidal geometry is triggered only for multiple harmonics RMPs and when Chirikov overlapping parameter $\sigma > 1$, which correspond to values of external resonant magnetic perturbation ψ_0 with island width $W_0 > 13$. In Fig. 10 we see for the three first values of W_0 , Q_{conv} stays practically constant as the value of $Q_{\delta B}$ increases. This corresponds to the situation where the Chirikov overlapping parameter is smaller than one. Comparing figure 4, 9 and 11 we see that even for different shapes and intensities of the equilibrium electric potential and convective fluxes, the poloidal rotation in all the three figures are at the same order of magnitude and have the

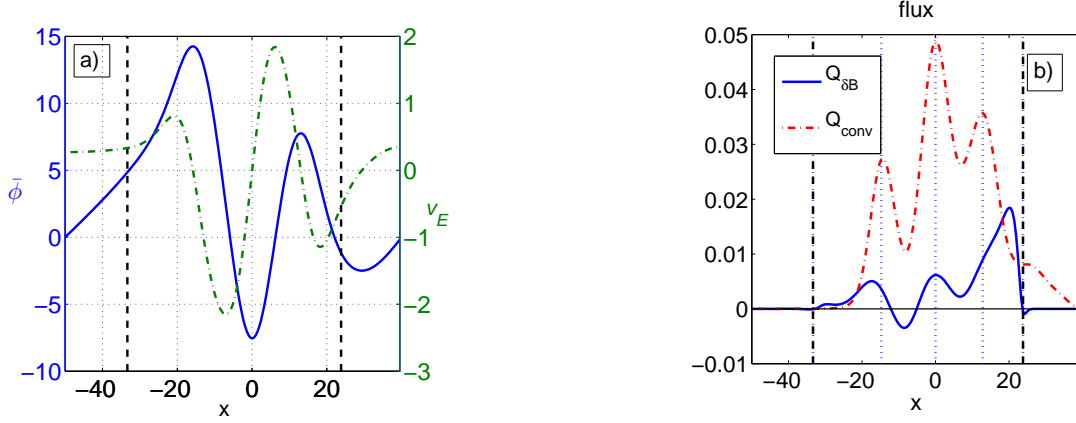


FIG. 9. (Color online) Multiple harmonics RMP for cylindrical curvature with island width $W_0 = 18.7$. Picture a) depicts the equilibrium electric potential and poloidal rotation $v_E(x)$, and we find in b) the difference in the flux intensities for Q_{conv} and $Q_{\delta B}$.

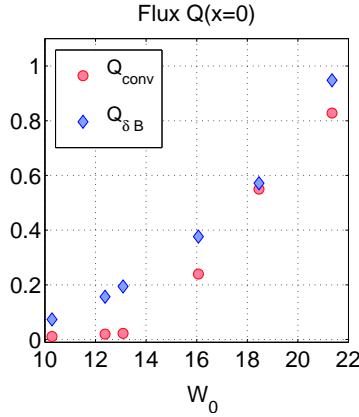


FIG. 10. (Color online) Radially integrated convective and flutter fluxes for the toroidal case, $Q_{conv} = \int_{q=2.5}^{q=3.5} Q_{conv}(x) dx$ and $Q_{\delta B} = \int_{q=2.5}^{q=3.5} Q_{\delta B}(x) dx$, as a function of multiple magnetic perturbations amplitudes expressed in terms of the vacuum island width W_0 . For low values of external resonant magnetic perturbation ψ_0 , which correspond to island width $W_0 < 13$ and Chirikov overlapping parameter $\sigma < 1$, Q_{conv} is smaller than $Q_{\delta B}$ and the poloidal rotation is absent.

maximum shear $|dv_E/dx|$ at the $q = 3$ resonant surface. This indicates that an important induced poloidal rotation can be controlled by the RMP currents.

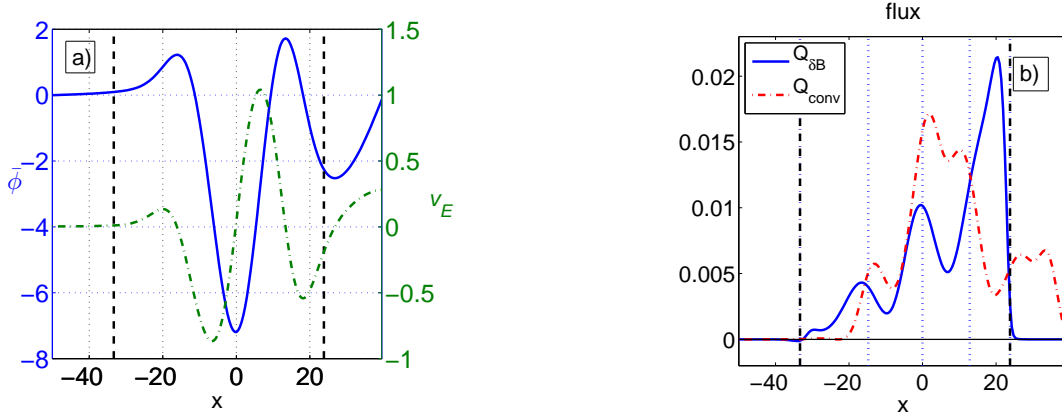


FIG. 11. (Color online) Multiple harmonics RMP for toroidal curvature island width $W_0 = 18.7$. As described in Fig. 9, a) depicts the equilibrium electric potential and poloidal rotation $v_E(x)$ and b) the difference in the flux intensities for Q_{conv} and $Q_{\delta B}$.

VI. CONCLUSIONS

In this work we investigate the dependence of the radial transport of the thermal energy from convection and magnetic flutter from the plasma response to a reference model of the resonant magnetic perturbations RMPs. The stationary states are studied running the 3D plasma edge turbulence code EMEDGE3D below to primary ballooning instability threshold. The simple static equilibrium in which the magnetic perturbation inside the plasma is in phase with the external perturbation and the plasma is not rotating is found to be unstable. The plasma is self-organized into a more complex state where the perturbation becomes phase shifted and the plasma rotates. This is due to the coupling between pressure and electrostatic potential perturbations induced by the magnetic curvature. In the stable equilibrium state, the phase between pressure and electrostatic potential is such that produces a rotating plasma with a significant thermal convective that exceeds the thermal flux from the magnetic flutter by a factor of 3–10 times. The instability of the simple equilibrium and the subsequent evolution to a new stable complex equilibrium has been first investigated in cylindrical geometry for a single harmonic RMP perturbation and latter for multiple RMP modes. We showed that for both situations the system reaches the same final equilibrium state with high convective flux and induced poloidal rotation. Then, we showed that the corresponding coupling mechanism between pressure and the electric potential also produces plasma rotation and a strong convective flux in the toroidal geometry with multiple

RMPs. The convective thermal flux and the magnetic flutter flux are about the same order of magnitude, but the presence of the thermal convective flux condition is only achieved when Chirikov overlapping parameter is greater than one.

ACKNOWLEDGMENTS

The authors gratefully acknowledge Wendell Horton and Iberê Caldas for useful discussions. This research was supported by the French National Research Agency, project ANR-2010-BLAN-940-01, and Brazilian national research agencies CNPq/CAPES under project No. 163395/2013-6 and FAPESP No. 201119296-1.

REFERENCES

- ¹F. Wagner, G. Becker, K. Behringer, D. Campbell, A. Eberhagen, W. Engelhardt, G. Fussmann, O. Gehre, J. Gernhardt, G. v. Gierke, G. Haas, M. Huang, F. Karger, M. Keilhacker, O. Klüber, M. Kornherr, K. Lackner, G. Lisitano, G. G. Lister, H. M. Mayer, D. Meisel, E. R. Müller, H. Murmann, H. Niedermeyer, W. Poschenrieder, H. Rapp, H. Röhr, F. Schneider, G. Siller, E. Speth, A. Stäbler, K. H. Steuer, G. Venus, O. Vollmer, and Z. Yü, *Phys. Rev. Lett.* **49**, 1408 (Nov 1982), <http://link.aps.org/doi/10.1103/PhysRevLett.49.1408>.
- ²J. W. Connor, R. J. Hastie, H. R. Wilson, and R. L. Miller, *Physics of Plasmas* **5**, 2687 (1998), <http://scitation.aip.org/content/aip/journal/pop/5/7/10.1063/1.872956> BibitemShutNoStop
- ³R. J. Groebner, T. Osborne, A. Leonard, and M. Fenstermacher, *Nuclear Fusion* **49**, 045013 (2009).
- ⁴J. W. Connor, *Plasma Physics and Controlled Fusion* **40**, 531 (1998), <http://stacks.iop.org/0741-3335/40/i=5/a=002>.
- ⁵M. Leconte, P. Beyer, X. Garbet, and S. Benkadda, *Physical Review Letters* **102**, 045006 (2009), <http://link.aps.org/doi/10.1103/PhysRevLett.102.045006>.
- ⁶M. Leconte, P. Beyer, X. Garbet, and S. Benkadda, *Nuclear Fusion* **50**, 054008 (2010).
- ⁷P. Beyer, F. de Solminihac, M. Leconte, X. Garbet, F. L. Waelbroeck, A. I. Smolyakov, and S. Benkadda, *Plasma Physics and Controlled Fusion* **53**, 054003 (2011).

- ⁸R. Fitzpatrick, *Physics of Plasmas* **2**, 825 (1995).
- ⁹G. Fuhr, P. Beyer, and S. Benkadda, *Physical Review Letters* **101**, 195001 (2008).
- ¹⁰P. Beyer, S. Benkadda, G. Fuhr-Chaudier, X. Garbet, P. Ghendrih, and Y. Sarazin, *Plasma Physics and Controlled Fusion* **49**, 507 (2007).
- ¹¹P. B. A. Monnier, G. Fuhr, *Nuclear Fusion* **Accepted for publication**, 000 (2014).
- ¹²B. Chirikov, *Physics Reports* **52**, 263 (1979).